Mushabbar A. Syed
Subha V. Raman
Orlando P. Simonetti
Editors

Basic Principles of Cardiovascular MRI

Physics and Imaging Technique

Springer

Basic Principles of Cardiovascular MRI

Mushabbar A. Syed • Subha V. Raman
Orlando P. Simonetti
Editors

Basic Principles of Cardiovascular MRI

Physics and Imaging Technique

Springer

Editors
Mushabbar A. Syed
Department of Medicine
Loyola University Medical Center
Maywood, IL
USA

Orlando P. Simonetti
The Ohio State University
Columbus, OH
USA

Subha V. Raman
The Ohio State University
Columbus, OH
USA

ISBN 978-3-319-22140-3 ISBN 978-3-319-22141-0 (eBook)
DOI 10.1007/978-3-319-22141-0

Library of Congress Control Number: 2015954859

Springer Cham Heidelberg New York Dordrecht London

Printed on acid-free paper

Springer International Publishing AG Switzerland is part of Springer Science+Business Media (www.springer.com)

To the source of my inspiration, my wife Humaira and my children Daneyal, Ameena, and Aleena.

Mushabbar A. Syed

To the mentors, colleagues, and students.

Subha V. Raman

To my loving wife, Lynn.

Orlando P. Simonetti

Preface

Cardiovascular magnetic resonance (CMR) has evolved into a routinely used imaging modality in clinical practice. Indications for CMR continue to expand which have led to the development of appropriate use criteria by the relevant medical societies including the American College of Cardiology, Society for Cardiovascular Magnetic Resonance, and the European Society of Cardiology. CMR is a relatively complex modality that requires good understanding of the basic principles including the relevant physics. Fellowship training programs have been developed to provide CMR training to cardiologists and radiologists using a combination of didactic teaching, clinical experience, and hands-on experience. Didactic training in the basic principles of CMR is mostly completed in the form of lectures and self-study. However, most of the available texts on MRI physics are not specific to CMR or are not up to date. The objective of writing this book was to develop a comprehensive and contemporary text on the basic principles and imaging techniques of CMR that will serve as a main reference source for both trainees and faculty. In doing so, we have chosen authors that are highly regarded as CMR experts, researchers, and teachers. Many authors direct CMR fellowship programs and are actively involved in training and education. We believe that this book will not only be useful for CMR fellowship trainees, cardiologists and radiologists who want to learn or expand their knowledge but also for CMR experts and physicists to use as a reference material.

The book is divided into two parts. Part one includes Chaps. 1 through 8 and focuses on the basic principles of CMR, MRI safety, and high field imaging. This part forms the basis for understanding of advanced techniques discussed in part two. Part two includes Chaps. 9 through 22 that discuss various techniques used in CMR including a review of advanced and emerging techniques. Tables and figures are included where appropriate and key references are included at the end of the chapter. This book is available in both print and electronic formats.

The success of any textbook depends on its ability to satisfy the needs of readers. We hope that readers will appreciate the clarity and thoroughness of each chapter and the hard work that went into developing this text. We will welcome any feedback comments to help improve the future editions.

Last but not the least, we want to extend our sincere thanks to Tracy Marton (Developmental Editor, Springer) for her invaluable help in completing this book and Grant Weston (Senior Editor, Medicine, Springer) for his insight, support, and overseeing this work to completion.

Maywood, IL, USA — Mushabbar A. Syed
Columbus, OH, USA — Subha V. Raman
Columbus, OH, USA — Orlando P. Simonetti

Contents

Contributors

Editors

Mushabbar A. Syed, MD, FACC Rolf & Merian Gunnar Professor of Medicine, Departments of Medicine – Cardiology, Radiology, Cell & Molecular Physiology, Director, Cardiovascular Imaging & Cardiology Fellowship Program, Stritch School of Medicine, Loyola University Medical Center, Maywood, IL, USA

Subha V. Raman, MD, MSEE, FACC, FAHA Professor and Joseph M. Ryan, MD Chair in Cardiovascular Medicine, Associate Division Director for Quality, and Medical Director, CMR/CT, The Ohio State University, Columbus, OH, USA

Orlando P. Simonetti, PhD, FISMRM, FAHA John W. Wolfe Professor in Cardiovascular Research, Professor of Cardiovascular Medicine and Radiology, Research Director, CMR/CT, The Ohio State University, Columbus, OH, USA

Contributors

Mehmet Akçakaya, PhD Department of Medicine, Beth Israel Deaconess Medical Center, Harvard Medical School, Boston, MA, USA

Anthony H. Aletras, PhD Department of Medicine, Laboratory of Medical Informatics, Aristotle University of Thessaloniki, Thessaloniki, Greece

Department of Clinical Physiology and Nuclear Medicine, Lund University Hospital, Lund, Sweden

Lara Bakhos, MD Department of Medicine-Cardiology, Stritch School of Medicine, Loyola University Medical Center, Maywood, IL, USA

Octavia Bane, PhD Departments of Biomedical Engineering and Radiology, Northwestern University, Chicago, IL, USA

Mount Sinai Hospital, Translational and Molecular Imaging Institute, New York, NY, USA

Xiaoming Bi, PhD MR R&D, Siemens Healthcare, Los Angeles, CA, USA

S. Bidhult, MSc Department of Clinical Physiology and Nuclear Medicine, Lund University Hospital, Lund, Sweden

Anja C.S. Brau, PhD GE Healthcare, Cardiac Center of Excellence, GE Global Research Center, Munich, Germany

Charles G. Cantrell Departments of Biomedical Engineering and Radiology, Northwestern University, Chicago, IL, USA

Department of Radiology, Northwestern Memorial Hospital, Chicago, IL, USA

Marcus Carlsson, MD, PhD Department of Clinical Physiology and Nuclear Medicine, Lund University Hospital, Lund, Sweden

Timothy J. Carroll, PhD Departments of Biomedical Engineering and Radiology, Northwestern University, Chicago, IL, USA

Department of Radiology, Northwestern Memorial Hospital, Chicago, IL, USA

Neil R. Chatterjee, BS Northwestern University Feinberg School of Medicine, Chicago, IL, USA

Yi-Cho Chung, PhD Paul C. Lauterbur Research Center for Biomedical Imaging, Shenzhen Institutes of Advanced Technology, Chinese Academy of Sciences, Shenzhen, China

Rohan Dharmakumar, PhD Biomedical Imaging Research Institute, Department of Biomedical Sciences, Cedars-Sinai Medical Center, Los Angeles, CA, USA

Department of Medicine and Bioengineering, UCLA, Los Angeles, CA, USA

Matthias Alexander Dieringer, PhD Department of Cardiology and Nephrology, Cardiovascular MRI – Experimental and Clinical Research Center, a joint cooperation between Charité Medical Faculty and Max-Delbrueck Center for Molecular Medicine, and HELIOS Clinics Berlin-Buch, Berlin, Germany

Robert R. Edelman, MD Department of Radiology, Evanston Hospital, NorthShore University HealthSystem, Evanston, IL, USA

NorthShore University HealthSystem, Evanston, IL, USA

Henrik Engblom, MD, PhD Department of Clinical Physiology and Nuclear Medicine, Lund University Hospital, Lund, Sweden

Pedro Filipe Ferreira, PhD Department of Cardiovascular BRU, Royal Brompton Hospital, London, UK

David N. Firmin, PhD Department of Cardiac MRI, Royal Brompton Hospital, London, UK

Oisin Flanagan, MD Northwestern University Feinberg School of Medicine, Chicago, IL, USA

NorthShore University HealthSystem, Evanston, IL, USA

Peter Gatehouse, PhD Department of Cardiac MRI, Royal Brompton Hospital, London, UK

Christopher J. Hardy, PhD GE Global Research, Niskayuna, NY, USA

Gregory R. Hartlage, MD Department of Internal Medicine, Division of Cardiology, Emory University, Atlanta, GA, USA

Ning Jin, PhD MR R&D, Siemens Healthcare, Columbus, OH, USA

Robert M. Judd, PhD Department of Medicine, Duke University Medical Center, Durham, NC, USA

Ioannis Koktzoglou, PhD Department of Radiology, Evanston Hospital, NorthShore University HealthSystem, Evanston, IL, USA

The University of Chicago Pritzker School of Medicine, Chicago, IL, USA

Arunark Kolipaka, PhD Department of Radiology, The Ohio State University Wexner Medical Center, Columbus, OH, USA

Herbert Köstler, PhD Department of Radiology, University of Würzburg, Würzburg, Germany

Daniel C. Lee, MD Department of Medicine, Division of Cardiology, Northwestern University Feinberg School of Medicine, Chicago, IL, USA

Ruth P. Lim, MD Department of Radiology, Austin Health, Melbourne/Heidelberg, VIC, Australia

The University of Melbourne, Melbourne, Victoria, Australia

Michael Loecher, PhD Department of Medical Physics, University of Wisconsin Madison, Madison, WI, USA

David Lopez, MD Department of Medicine, Cardiovascular Division, University of Virginia Health System, Charlottesville, VA, USA

Sophie Mavrogeni, MD, FESC Department of Cardiology, Onassis Cardiac Surgery Center, Athens, Attiki, Greece

Raad H. Mohiaddin, MD, FRCR, FRCP, FESC, PhD Department of Cardiology and Imaging, Royal Brompton Hospital, National Heart and Lung Institute, Imperial College London, London, UK

Reza Nezafat, PhD Department of Medicine, Beth Israel Deaconess Medical Center, Harvard Medical School, Boston, MA, USA

John N. Oshinski, PhD Radiology and Imaging Sciences, Emory University School of Medicine, Atlanta, GA, USA

Ronald Ouwerkerk, PhD The Biomedical and Metabolic Imaging Branch, National Institute of Diabetes and Digestive and Kidney Diseases (NIDDK), Bethesda, MD, USA

Elena Peña, MD Department of Radiology, University of Ottawa, Ottawa, ON, USA

Department of Medical Imaging, The Ottawa Hospital, Ottawa, ON, Canada

Anurag Sahu, MD Division of Cardiology, Emory University Hospital, Atlanta, GA, USA

Michael Salerno, MD, PhD Department of Medicine, Cardiovascular Division, Radiology and Biomedical Engineering, University of Virginia Health System, Charlottesville, VA, USA

Haris Saybasili, PhD MR R&D, Siemens Healthcare, Chicago, IL, USA

John F. Schenck, MD, PhD GE Global Research, Niskayuna, NY, USA

Jeanette Schulz-Menger, MD Department of Cardiology and Nephrology, Cardiovascular MRI – Experimental and Clinical Research Center, a joint cooperation between Charité Medical Faculty and Max-Delbrueck Center for Molecular Medicine, and HELIOS Clinics Berlin-Buch, Bavaria, Germany

Nicole Seiberlich, PhD Biomedical Engineering, Case Western Reserve University, Cleveland, OH, USA

Behzad Sharif, PhD Biomedical Imaging Research Institute, Department of Biomedical Sciences, Cedars-Sinai Medical Center, Los Angeles, CA, USA

Suzanne Smart, BS Davis Heart and Lung Research Institute, Ohio State University Wexner Medical Center, Columbus, OH, USA

Rebecca E. Thornhill, PhD Department of Radiology, University of Ottawa, Ottawa, ON, Canada

Clinical Epidemiology Program, Ottawa Hospital Research Institute, Ottawa, ON, USA

Department Medical Imaging c/o Laura Lang, The Ottawa Hospital, Civic Campus, Ottawa, ON, USA

Johannes Tran-Gia, PhD Department of Radiology, University of Würzburg, Würzburg, Germany

Parmede Vakil, PhD Departments of Biomedical Engineering and Radiology, Northwestern University, Chicago, IL, USA

Department of Radiology, Northwestern Memorial Hospital, Chicago, IL, USA

Florian von Knobelsdorff-Brenkenhoff, MD, PhD Department of Cardiology and Nephrology, Cardiovascular MRI – Experimental and Clinical Research Center, a joint cooperation between Charité Medical Faculty and Max-Delbrueck Center for Molecular Medicine, and HELIOS Clinics Berlin-Buch, Berlin, Germany

David C. Wendell, PhD Department of Medicine/Cardiology, Duke University Medical Center, Durham, NC, USA

Oliver Wieben, PhD Departments of Medical Physics and Radiology, University of Wisconsin School of Medicine and Public Health, Madison, WI, USA

Christos G. Xanthis, PhD Department of Computer Science and Biomedical Informatics, University of Thessaly, Lamia, Greece

Hsin-Jun Yang, MS Biomedical Imaging Research Institute, Department of Biomedical Sciences, Cedars-Sinai Medical Center, Los Angeles, CA, USA

Department of Bioengineering, UCLA, Los Angeles, CA, USA

Part I

Basic Principles of Magnetic Resonance Imaging

Signal Generation

1

Arunark Kolipaka

Abstract

This chapter provides some basic information regarding the origin of the MRI signal. The MRI signal is generated by the interaction of applied magnetic fields with the nuclei of hydrogen atoms in the body. Hydrogen nuclei (protons, or "spins") tend to align themselves with the large static magnetic field generated by the MRI system, and rotate or precess about the direction of that field at a characteristic frequency called the Larmor frequency. The application of additional radiofrequency (RF) energy at the same frequency excites the magnetized protons causing them to tip into the plane perpendicular to the main field. The magnetized protons which have been perturbed in this fashion undergo a process of relaxation that returns them back into alignment with the main field. During the course of relaxation, a signal is emitted which is detected using receiver coils and digitally sampled. The relaxation of spins is governed by time constants known as T_1 and T_2, and these time constants play a major role in determining the contrast between tissues in an image. The encoding of spatial information is accomplished using magnetic field gradients that alter the precession frequency of spins based on their position in the scanner. The Fourier transform is then used to reconstruct an image from the encoded data. Many of the basic concepts introduced in this chapter are covered in greater detail in later chapters.

Keywords

Larmor Frequency • T_1 relaxation • T_2 relaxation • Spatial encoding • Bloch Equations • Slice selection gradient • Phase encoding gradient • Readout gradient

The Magnetic Resonance Imaging (MRI) signal is generated by the hydrogen nuclei (protons) in human tissue. Three fourths of the human body consists of water, and each water molecule includes two hydrogen atoms; thus, water is the primary source of MRI signal in medical imaging applications. This chapter covers the important steps required to generate the signal used to create MR images.

A. Kolipaka, PhD
Department of Radiology, The Ohio State University Wexner Medical Center, 395 W 12th Ave, 4th Floor Radiology, Columbus, OH 43210, USA
e-mail: arunark.kolipaka@osumc.edu

The MRI Signal

Any modern digital imaging system requires a probe to interact with the tissue to be imaged; this interaction results in a signal that is detected, digitized, and further processed to generate an image as shown in Fig. 1.1. In magnetic resonance imaging (MRI), radiofrequency (RF) pulses are used to excite the tissue, and the resulting signal is detected by receiver coils. MRI is thus based on the absorption and emission of energy in the RF range of the electromagnetic spectrum. Although several chemical elements can interact with magnetic fields to emit an MRI signal, the large amount of hydrogen found in the body, and the relatively large signal it produces, has made hydrogen-based the most widely used MRI technique for clinical

M.A. Syed et al. (eds.), *Basic Principles of Cardiovascular MRI: Physics and Imaging Technique*,
DOI 10.1007/978-3-319-22141-0_1

diagnosis. The primary sources of MRI signal in the human body are the hydrogen nuclei found in tissues comprised mainly of water, and also fat (hydrocarbons). In the following discussion, the terms “hydrogen nuclei,” “protons,” and “spins” will be used interchangeably to describe the atomic particles that provide the primary source of the MRI signal.

Nuclear Spin in a Magnetic Field

Hydrogen has a nuclear property known as “spin” that results in a magnetic moment, μ. Because of this magnetic moment, when exposed to the static magnetic field (B_0) generated by the main magnet of the MRI system, hydrogen nuclei will align parallel or anti-parallel to the field as shown in Fig. 1.2. The energy difference (E) between these two orientations is $E=2\mu B_0$. The small preference for the hydrogen nuclei to align toward the parallel, lower energy state, over the anti-parallel orientation, contributes to the development of the net longitudinal magnetization [1]. The net magnetization is the vector sum of magnetic moments from many individual protons.

Larmor Frequency

When a hydrogen nucleus is exposed to a magnetic field of strength B_0, it precesses at a frequency, ω, due to the interaction of its angular momentum and the field, as illustrated in Fig. 1.3. The frequency, ω, depends on B_0 and on the gyromagnetic ratio, γ, of the specific nucleus according to the Larmor Eq. 1.1.

$$\omega_L = \gamma B_0 \tag{1.1}$$

For hydrogen nuclei, $\gamma/2\pi = 42.58$ MHz/T, and ω_L is termed the Larmor frequency. Thus, the Larmor frequency of precession is dependent on the applied magnetic field strength; for example, protons will precess at approximately 64 MHz at 1.5T, and 128 MHz at 3.0T.

Excitation of Spins

In a three-dimensional (x, y, z) coordinate system, let us assume by convention that the static magnetic field is oriented in the z-direction. As a result, the net longitudinal magnetization vector at equilibrium (M_0) will point in the z-direction as shown in Fig. 1.4a; this is due to the alignment of a majority of protons with the applied field.

Protons can be excited to the higher energy state by applying a radio frequency (RF) field oscillating at the

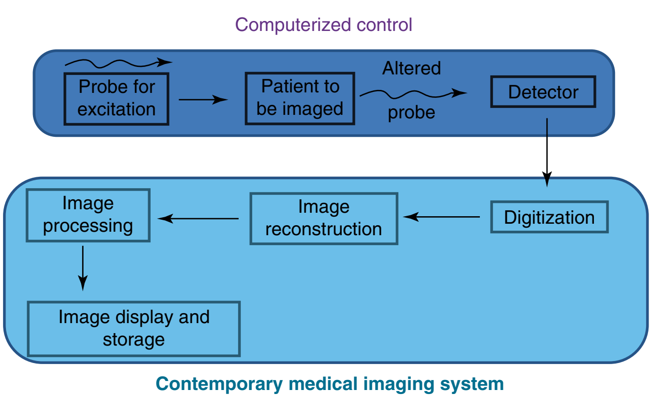

Fig. 1.1 The generic process behind any modern medical imaging system, including MRI

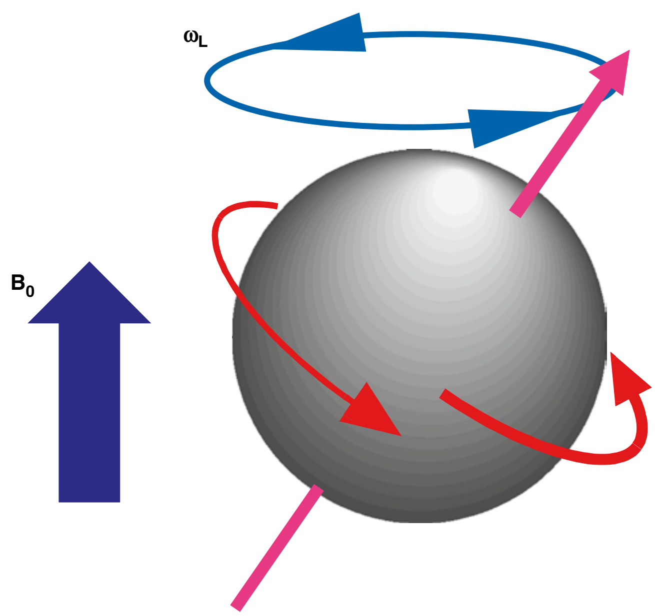

Fig. 1.3 Spins precess at a frequency, ω, that depends on the externally applied magnetic field, B_0, and the gyromagnetic ratio, γ, of the particular nuclei. The gyromagnetic ratio for hydrogen is 42.58 MHz/T

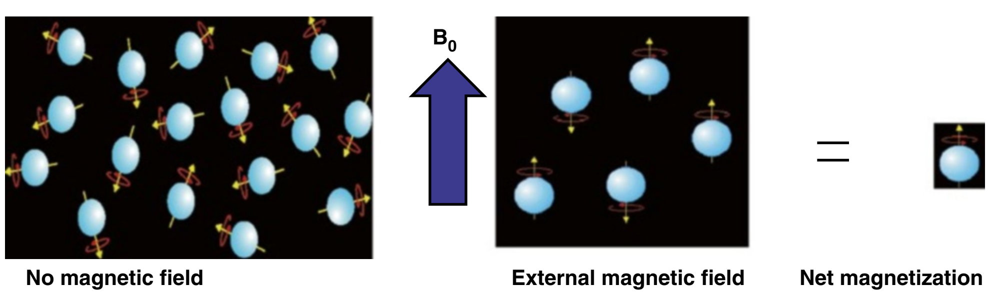

Fig. 1.2 The alignment of a majority of spins (hydrogen nuclei, i.e., protons) with a strong magnetic field generates a net longitudinal magnetization

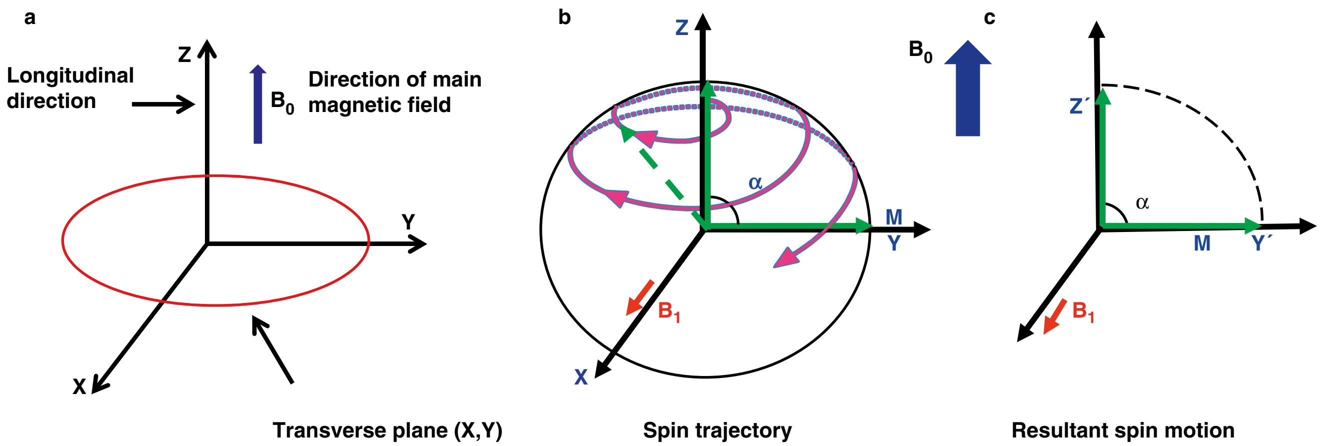

Fig. 1.4 Schematics showing (**a**) the direction of the main magnetic field and longitudinal magnetization, (**b**) nutation of a spin from the longitudinal axis to the transverse plane in response to an applied RF field (B_1) (**c**) the final result of tipping all of the longitudinal magnetization by flip angle $\alpha = 90°$ into the transverse plane

Larmor frequency; this applied RF field is known as the B_1 field. The magnitude of the net longitudinal magnetization in the z-direction is extremely small compared to the magnetic field strength, B_0, and is undetectable. In order to measure a detectable signal from protons, the magnetization is tipped out of alignment with B_0 and into the transverse plane. When an RF pulse is applied at the Larmor frequency, i.e., a B_1 field is switched on briefly as shown in Fig. 1.4b, the net magnetization vector will respond and be tipped away from the z-axis and towards the x-y transverse plane (Fig. 1.4c). The angle that the magnetization vector rotates away from the z-axis is known as flip angle (α), and can be approximated as

$$\alpha = \gamma \tau B_1 \tag{1.2}$$

where τ represents the length of time the RF pulse is applied with amplitude B_1.

When the RF pulse is terminated, the net magnetization will begin to return back to the longitudinal axis as the protons return to equilibrium by releasing energy to the environment, a process known as relaxation as termed by Felix Bloch, one of the discoverers of the nuclear magnetic resonance phenomenon that forms the basis for MRI. Before the protons fully relax back to equilibrium, the signal generated by the transverse component of the precessing magnetization can be detected using an RF receiver coil.

MR Signal and Contrast Characteristics from Spin Relaxation

The MRI signal available from stationary tissue is determined by a combination of factors, including the density of protons and their relaxation rates; depending on the specific pulse sequence parameters, the image contrast will reflect these as well as many other factors such as flow and motion, diffusion, local differences in magnetic susceptibility and field homogeneity. Two types of relaxation take place: longitudinal, spin-lattice or T_1 relaxation, and transverse, spin-spin, or T_2 relaxation. The extent that T_1 and T_2-relaxations and proton density contribute to image intensity and contrast is controlled through manipulation of pulse sequence timing and RF pulse flip angles as explained in later chapters.

Longitudinal Relaxation (Spin-Lattice Relaxation)

The spin lattice relaxation time, or T_1, is the characteristic tissue-specific exponential time constant that governs the regrowth of longitudinal magnetization (M_z) towards its equilibrium value, M_0 (Fig. 1.5). T_1 is the time required for M_z to regain 63 % of its equilibrium value when starting from zero, e.g., following the application of a 90° excitation pulse that tips the longitudinal magnetization completely into the transverse plane; this can be expressed as:

$$M_Z = M_0\left(1 - e^{-t/T1}\right) \tag{1.3}$$

where *t* is the time following the excitation pulse.

Longitudinal, spin-lattice relaxation is caused by the transfer of thermal energy between excited nuclei and the surrounding atomic lattice [2]. Molecules that have an efficient means of energy transfer will exhibit a shorter T_1 relaxation time, while those without effective transfer mechanisms demonstrate a longer T_1 time. This is primarily dependent on the mobility of the lattice, and the related vibrational and rotational frequencies. The more closely these frequencies correspond to the energy gap, E, and the Larmor frequency, the more efficient is T_1 relaxation. Thus, T_1 relaxation is highly dependent on molecular motion, and

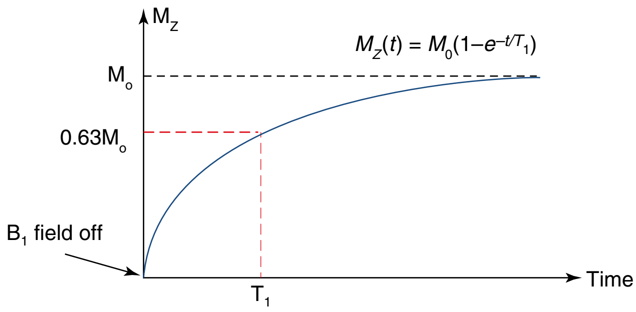

Fig. 1.5 Schematic illustrating T_1 recovery curve. T_1 relaxation constant defines the time to regain 63 % of longitudinal magnetization following a 90° excitation pulse

hence, on the size of the molecules. The motion of very large molecules generally occurs at a frequency too low for efficient energy transfer, and likewise extremely mobile nuclei such as those in free water are moving at frequencies too high to facilitate relaxation; thus the T_1 values of fluids are relatively long, while fat tissues demonstrate shorter T_1 values [3].

T_1 Differences Determine Image Contrast

As an example, consider tissues A and B shown in Fig. 1.6; tissue A has a shorter T_1 relaxation time than tissue B, i.e., the longitudinal magnetization of tissue A will recover and realign with the main magnetic field more quickly than tissue B following RF excitation. After a 90° RF pulse, the magnetization vectors for both tissues A and B are tipped into the transverse plane and from there the longitudinal magnetization begins to recover. Magnetic resonance imaging typically requires multiple excitation pulses to collect all of the data needed to form an image; if the next excitation pulse is applied before full recovery occurs (which takes approximately five times T_1), tissue A will have recovered more longitudinal magnetization than tissue B. Since tissue A has a larger longitudinal component prior to the next RF pulse, it will have a larger transverse component after the RF pulse, and therefore tissue A will have a higher signal than tissue B, and will appear brighter in the image as shown in Fig. 1.6. Thus, in a pulse sequence designed to generate image contrast sensitive to T_1, i.e., a T_1-weighted image [4], tissues with shorter T_1 will have higher signal than tissues with longer T_1. Table 1.1 shows the T_1 values for various tissues at 1.5T [5].

Transverse Relaxation (Spin – Spin Relaxation)

The transverse magnetization created when an RF pulse is used to tip the longitudinal (M_z) magnetization into the transverse plane decays back to zero after the termination of the RF excitation pulse. The time constant, T_2, describes the

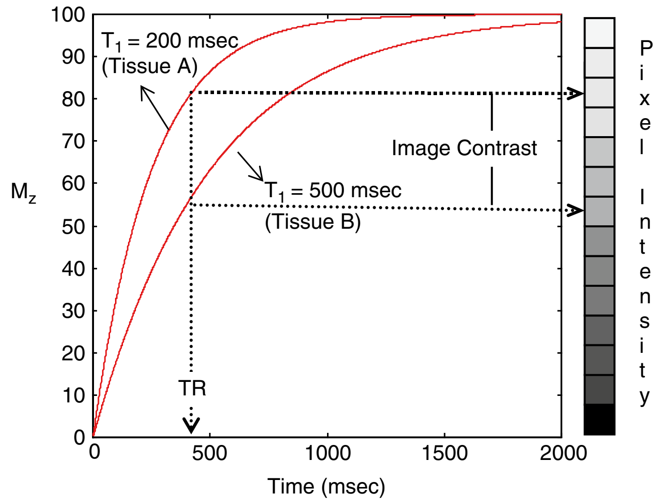

Fig. 1.6 Difference in T_1 relaxation times between example tissues A (T_1=200 ms) and B (T_1=500 ms) leads to a difference in longitudinal magnetization at time TR. This difference is used to generate contrast between the tissues in a T_1-weighted image

Table 1.1 Typical T_1 and T_2 values for various tissues at 1.5 T

Tissue	T_2 (ms)	T_1 (ms)
Adipose tissue	80	260
Liver	40	490
Skeletal muscle	50	870
Myocardium	60	950
Blood	~180 (arterial)	1500
Cerebrospinal fluid	2000	4200

exponential rate of decay of the transverse magnetization (Fig. 1.7), which is given by:

$$M_{xy}(t) = M_{xy}(0) * e^{-t/T_2} \tag{1.4}$$

where t is the time following the excitation pulse, and M_{xy} is the component of the magnetization in the transverse plane. By this equation, T_2 is the time required for 63 % of the initial transverse magnetization to dissipate [6, p. 381].

Recall that the net magnetization vector is the sum of magnetic moments from many individual protons. To maintain a detectable net transverse magnetization, the protons must maintain phase coherence, that is, they must precess in phase with one another at exactly the same frequency. Over time, however, the individual precessing protons get out of sync with each other, or become "dephased" in the transverse plane; this means that the individual magnetic moments begin to point in different directions, decreasing the total net transverse magnetization [3]. Realizing from the Larmor Equation (Eq. 1.1) that the precession frequency of a proton is dependent on the magnetic field it experiences, it is easy to understand that the primary reasons for transverse dephasing are related to spatial and temporal variations in the magnetic field. One

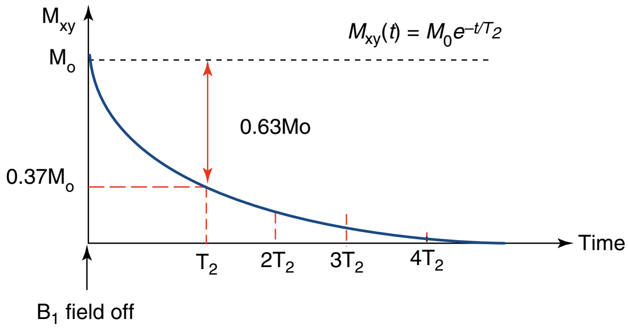

Fig. 1.7 Schematic illustrating T_2 decay curve. T_2 relaxation constant defines the time for transverse magnetization to decay to 37 % of its original value following an RF excitation pulse. T_2 is always shorter than T_1

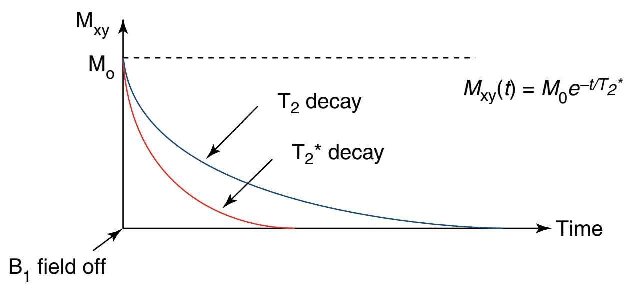

Fig. 1.8 T_2* takes into account local, static field inhomogeneities, as well as spin-spin relaxation, and therefore is always shorter than T_2

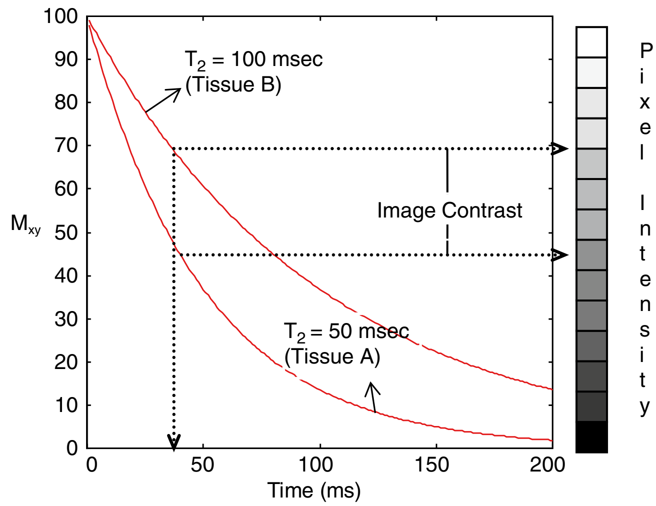

Fig. 1.9 Difference in T_2 relaxation times between example tissues A (T_2 = 50 ms) and B (T_2 = 100 ms) leads to a difference in transverse magnetization at time TE. This difference is used to generate contrast between the tissues in a T_2-weighted image

of the factors contributing to the dephasing of the protons is the interaction between the magnetic fields of individual protons, or so-called "spin-spin" dephasing [6]. Similar to spin-lattice relaxation, spin-spin relaxation is inefficient in highly mobile protons, and thus the T_2 relaxation time tends to be longer in free water, and in tissue containing a high percentage of water. Besides these temporally varying spin-spin interactions, transverse phase coherence is also affected by static inhomogeneties in the local magnetic field; these can be caused by inhomogeneities in the applied field, or by local differences in the magnetization of tissues due to differences in their magnetic susceptibility. The effective transverse relaxation time (T_2*) describes the exponential decay in signal that results from the combination of spin-spin relaxation (T_2) and static field inhomogeneties (T_2') [3] as shown in Fig. 1.8 and in the equation:

$$1/T_2^* = 1/T_2 + 1/T_2' \qquad (1.5)$$

T_2 Differences Determine Image Contrast

Again, consider an example of two tissues, tissue A and tissue B; let tissue A have a shorter T_2 time than tissue B, indicating that its transverse magnetization relaxes or decays more rapidly than tissue B. At any time following an excitation pulse, the amount of transverse magnetization in tissue A is less than tissue B, thus generating less signal in the image [4] as shown in Fig. 1.9. Thus, in a T_2-weighted image, tissues with longer T_2 will appear brighter than tissues with shorter T_2. Table 1.1 shows the T_2 relaxation times for different tissues.

Contrast Produced by Proton Density

Besides the tissue relaxation rates, contrast between tissues is also governed by differences in proton density. Proton density, as one would expect, is indicative of the number of protons per volume of tissue. The higher the number of protons in a given volume of tissue, the greater is the magnetization available to provide signal. Imaging pulse sequences can be designed to provide "proton density weighting," i.e., to be sensitive to proton density and relatively insensitive to T_1 or T_2 relaxation [4], although this contrast mechanism is rarely used in cardiovascular MRI applications.

Signal Acquisition

Free Induction Decay

In the most basic example of a nuclear magnetic resonance signal, a 90° RF pulse is applied to rotate the net longitudinal magnetization vector completely into the x-y plane, where it can induce a signal in an RF receiver coil. This signal, which is a result of the free precession of the net magnetization in the transverse plane, is called the free induction decay, or FID, since it gradually decays due to the relaxation mechanisms previously described.

The FID in hydrogen magnetic resonance has the following characteristics:

1. It oscillates at the Larmor frequency determined by the gyromagnetic ratio of hydrogen, and the applied magnetic field strength.
2. It has an initial magnitude that is proportional to the density of protons (hydrogen nuclei) in the sample being measured.
3. It decreases in amplitude exponentially with a time constant T_2*, due to the combination of spin-spin relaxation and magnetic field inhomogeneties [2].

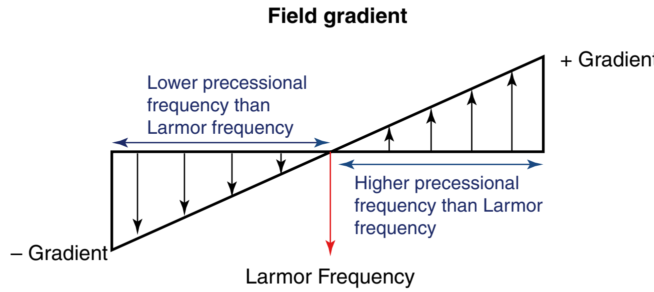

Fig. 1.10 Magnetic gradient field superimposes on the main magnetic field (B_0) to create a linear variation in field strength in the direction of the gradient. By the Larmor equation, this creates a linear variation in precessional frequencies as a function of location. This control over the spatial distribution of precessional frequencies enables spatial localization of the MR signal, and image encoding

Imaging Procedure

To generate an image, a sequence of RF pulses in combination with magnetic field gradients is implemented as detailed in later chapters. The specific sequence and timing of RF pulses, magnetic field gradient pulses, and delay times is designed to manipulate the transverse and longitudinal magnetization to generate a specific type of image contrast. It is typically necessary to repeat a pulse sequence a number of times to acquire enough data to form an image. Therefore, the time for one cycle of a pulse sequence is called the repetition time, or TR.

Spatial Localization

It is necessary to encode the emitted signal so that the spatial position of the nuclei contributing to the signal can be located through the image reconstruction process. To spatially encode the signal, sets of magnetic field gradients are applied during the imaging procedure. Using coils that are embedded in the bore of the MRI scanner, it is possible to superimpose a magnetic field gradient (variation in the magnetic field with respect to position) onto the static main magnetic field. These gradients are weaker magnetic fields oriented in the same direction as the B_0 field (i.e., the z-direction) and vary linearly with position. There are three independent gradient coils in the MRI system, each designed to create a linear variation in the static field along one of the Cartesian axes, x, y, and z; the gradients produced on each axis are respectively referred to as G_x, G_y, and G_z. Note that a linear gradient can be generated in any direction by appropriate combination of gradients along multiple axes simultaneously. This is what gives MRI the flexibility to generate images in any orientation.

As an example, G_x refers to a one-dimensional gradient superimposed on the B_0 field that causes a linear variation in the field in the x direction. In Fig. 1.10, the length of the vectors represents the magnitude of the gradient field that changes positively and negatively. Recalling that the Larmor Equation (Eq. 1.1) states that the precessional frequency is proportional to magnetic field strength, the gradient causes the precessional frequency to vary as a function of position along the direction of the gradient. Thus, the position of a particular spin along the direction of an applied gradient can be determined from its precessional frequency.

The imaging process can be divided into four fundamental operations:

1. Slice selection
2. Spatial encoding
3. Signal read-out
4. Image Reconstruction

Slice Selection

The slice selection gradient (G_z, by convention) and the RF pulse are applied simultaneously in order to excite (tip) the magnetization of protons only within a slice of discrete thickness (Fig. 1.11). The slice thickness is controlled by two factors: the amplitude of the magnetic field gradient, which affects the spatial distribution of the proton resonant frequencies, and the bandwidth of the RF pulse (i.e., the range of frequencies included in the pulse) [5] as shown in Fig. 1.12. We can see by Eq. 1.6,

$$\Delta z = \frac{2\pi \Delta f}{\gamma \vec{G}_z} \tag{1.6}$$

that the slice thickness, Δz, is proportional to the RF pulse bandwidth, Δf, and inversely proportional to the slice select gradient amplitude, G_z. That is, for a given bandwidth RF pulse, a stronger slice select gradient will excite a thinner

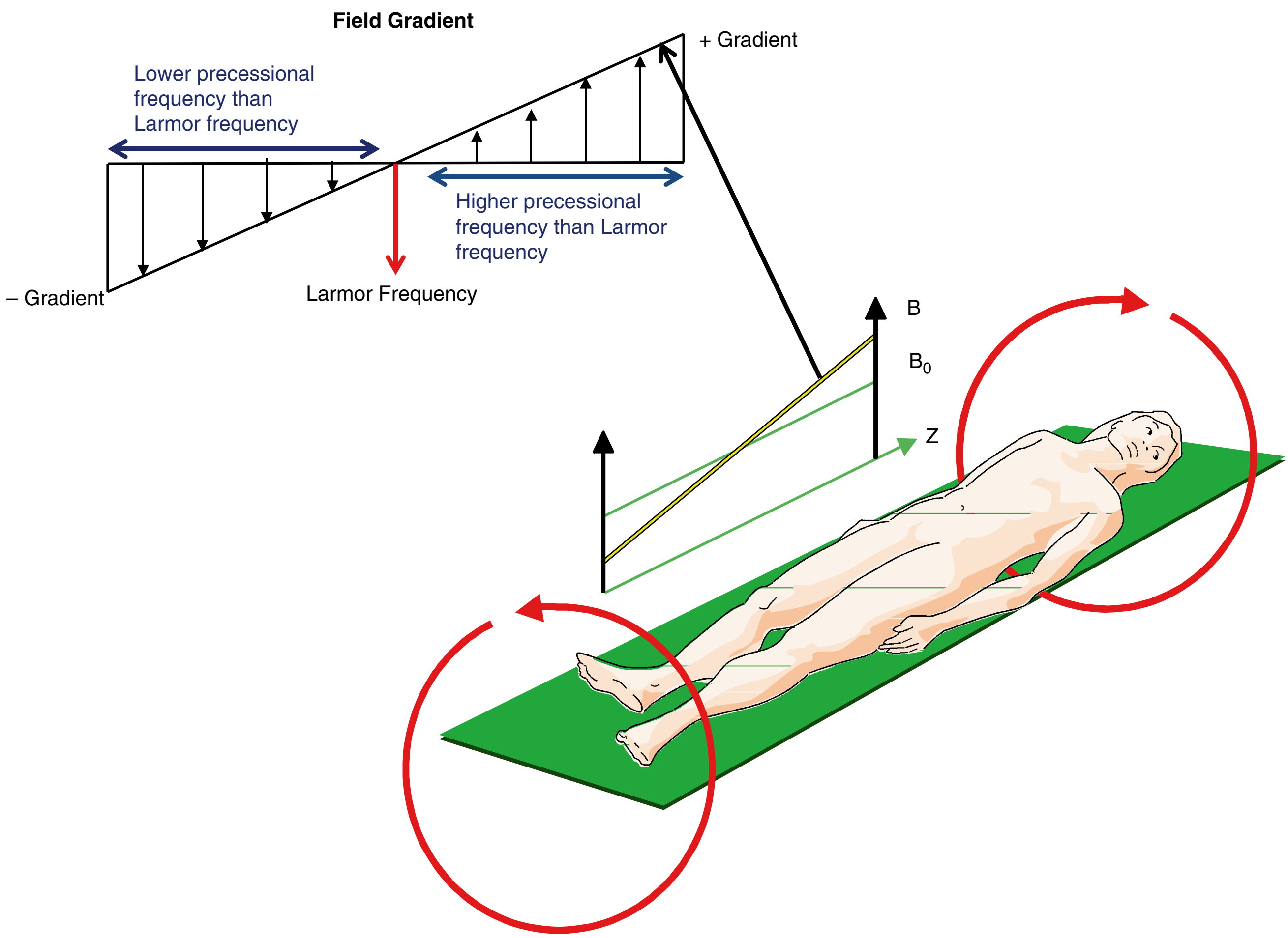

Fig. 1.11 Z-gradient coil, schematically represented by the red loops, generates a linear variation in the main magnetic field in the head to foot direction. Additional gradient coils create linear variations in the main field in X and Y directions. Using all three coils it is possible to select and encode an image in any orientation

slice as compared to a weaker slice gradient, as shown in Fig. 1.13. The center frequency of the RF pulse is set to match the precessional frequency of protons at the location of the desired slice, as shown in Fig. 1.14. Therefore, the slice select gradient localizes the signals in one direction.

Spatial Encoding

The next step in the process of image formation is to localize the positions of the protons within the slice (that is, in the in-plane x- and y-directions). Two gradients are applied, one (G_y) in the phase-encoding direction (by convention, the y-direction) and one (G_x) in the frequency-encoding direction (by convention, the x-direction). The latter is also called the "read-out gradient", because the signal is read or received during its application. When a phase-encoding gradient, G_y, is applied, the frequencies in the y direction are changed spatially. Similarly, when G_x is applied the frequencies in the x direction are changed spatially. This combination of gradients provides the basis for the application of the inverse two-dimensional Fourier transform ($M(k_x, k_y)$) which reconstructs the final image as shown in Eq. 1.7

$$M\left(k_x,k_y\right)=\int_x\int_y m\left(x,y\right)e^{-i2\pi\left[k_x x+k_y y\right]}dxdy \qquad (1.7)$$

where k_x and k_y are spatial frequencies in the x and y directions respectively. The time integrals of the applied gradients, G_x and G_y, control the sampling of spatial frequencies, k_x and k_y, as shown in Eqs. 1.8 and 1.9;

$$k_x=\frac{\gamma}{2\pi}\int_0^t G_x\left(t\right)dt \qquad (1.8)$$

$$k_y=\frac{\gamma}{2\pi}\int_0^t G_y\left(t\right)dt \qquad (1.9)$$

These relationships between gradient pulses and k-space sampling will be described in more detail in later chapters.

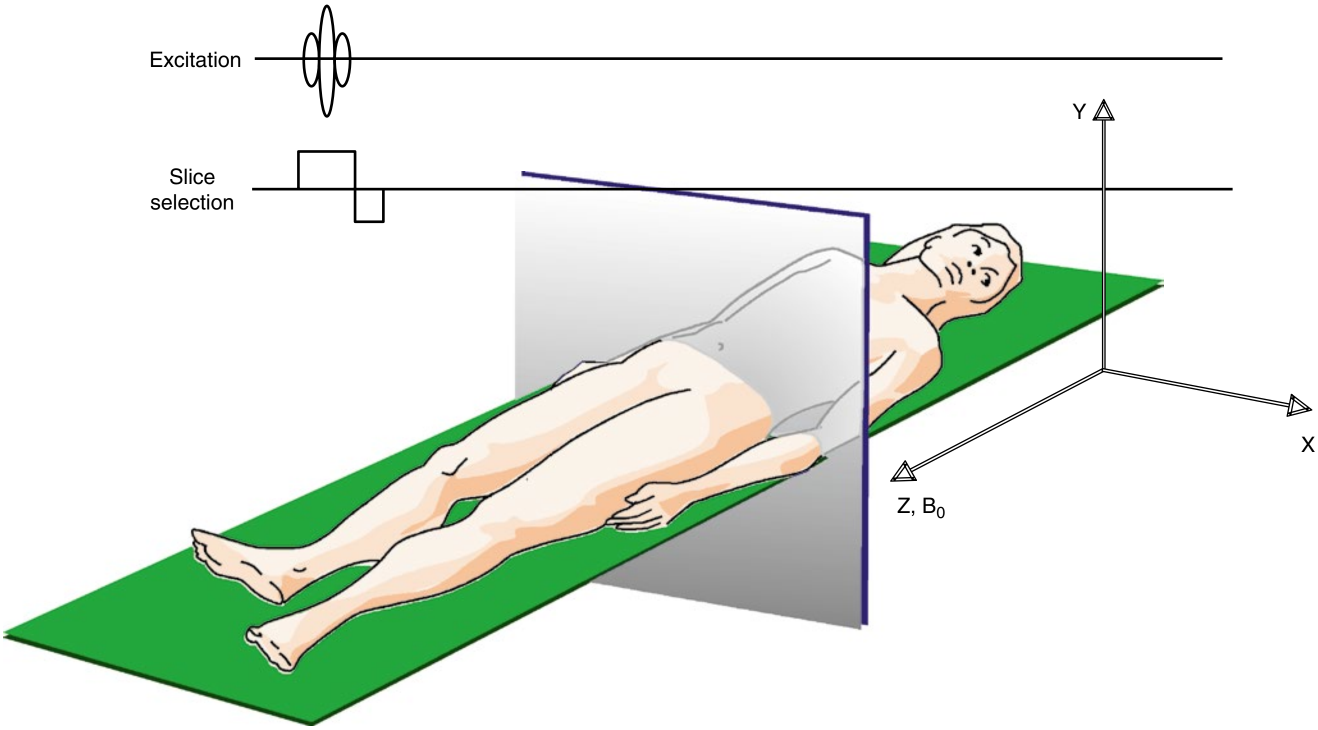

Fig. 1.12 RF excitation and slice select gradient are applied simultaneously to excite the spins only in the selected slice. The gradient creates a distribution of precessional frequencies along the direction of the gradient, and a narrow band RF pulse is applied to excite spins only within a location based on their frequency

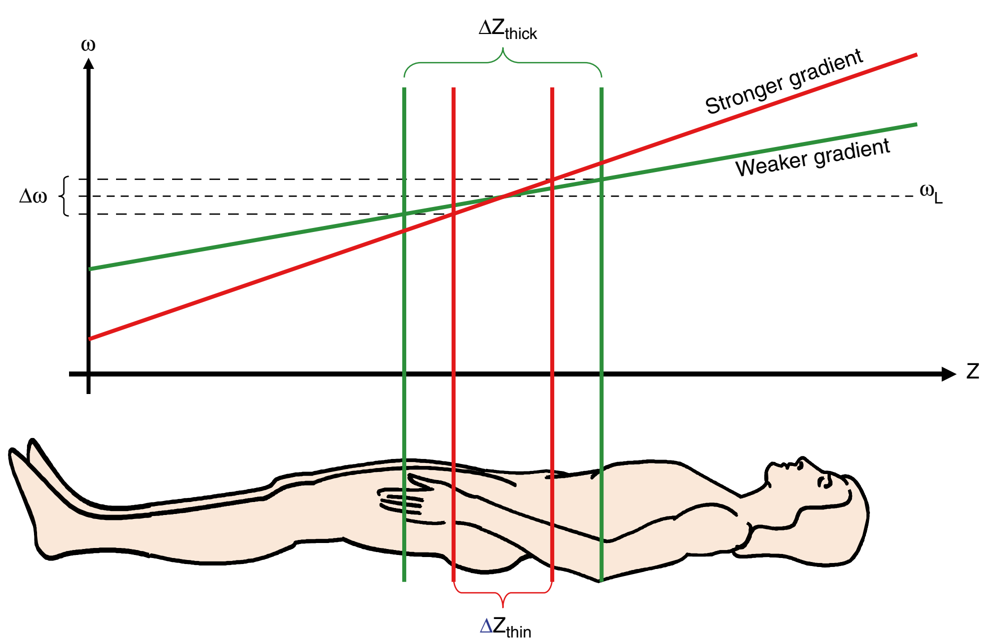

Fig. 1.13 Bandwidth of the RF pulse and the gradient strength (steepness of the change in magnetic field) together determine the thickness of the selected slice. For a given bandwidth RF pulse, the stronger gradient (*red line*) will excite a thinner slice compared to the weaker gradient (*green line*)

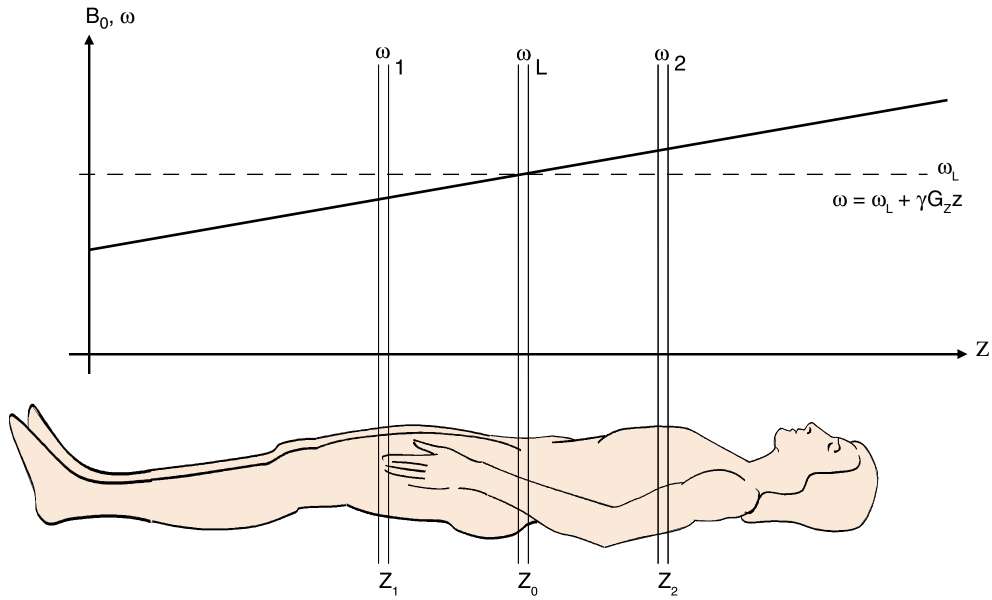

Fig. 1.14 The gradient creates a variation in magnetic field, which creates a variation in precessional frequency by the relationship described by the Larmor equation. This schematic shows how slices can be selected in different locations (z_1, z_0, z_2) by matching the frequency of the RF excitation pulse to the precessional frequency (ω_1, ω_0, ω_2) of spins in a specific location

Signal Read-out

The MRI signal is sampled during the G_x gradient application. The time-varying signal is digitized and stored in a two-dimensional data matrix known as k-space. As will be described in detail in the following chapters, spatial frequencies k_x and k_y define the axes of k-space. The sampled signal typically fills k-space one row, or k_x-line, at a time. Low spatial frequency data fill the center of k-space and provide information about general shapes and contrast in the image, while high spatial frequency data are stored in the periphery of k-space that represents image resolution and detail.

Image Reconstruction

In its most basic form, MR images are reconstructed by applying a two-dimensional Fourier transform to the raw k-space data row by row and column by column. This process effectively decodes the spatial position of the excited hydrogen nuclei based on variations in frequency and phase [2]. In the reconstruction process, a relative signal intensity value for each image voxel, or volume element, is calculated based on the strength of the signal from the hydrogen nuclei contained in the corresponding volume of tissue within the patient. The result is the final image, which illustrates spatial anatomical relationships and grayscale contrast between tissues based on the magnetization behavior of hydrogen within a slice of tissue [5]. Additional details on the process of image reconstruction are provided in the following chapters.

References

1. Slichter CP. Principles of magnetic resonance. 3rd ed. Berlin: Springer-Verlag; 1990.
2. Nishimura DG. Principles of magnetic resonance imaging. 11th ed. Raleigh: Lulu.com; 2010.
3. Elster AD, Burdette JH, editors. Questions and answers in magnetic resonance imaging. 2nd ed. Maryland Heights: Mosby; 1994.
4. Bushberg JT, et al. The essential physics of medical imaging. Philadelphia: Lippincott Williams & Wilkins; 1994.
5. Bernstein AM, et al. Hand book of MRI pulse sequences. Amsterdam: Elsevier; 2004.
6. Sprawls P. Physical principles of medical imaging. Philadelphia: Lippincott Williams & Wilkins; 1987.

k-Space

2

Michael Loecher and Oliver Wieben

Abstract

This chapter will introduce the k-space formalism used in MR imaging for data encoding and image reconstruction via Fourier transforms (FT). Essentially, this formalism is a mathematical construct that allows for the description of acquired MRI data in a domain described as spatial-frequency space, or k-space, which is related to the desired image space representation via the Fourier transform. Representing the data as k-space converts the time varying signal acquired with the MR receiving coils into a 2D or 3D data space that can be readily reconstructed into an image representation by applying the well-known Fourier transform. Understanding MRI acquisitions and reconstructions in terms of k-space is a crucial step in understanding the basic relationships between the acquisition and the reconstructed images, most acceleration and reconstruction techniques, sources of artifacts and their appearance, and advanced acquisition strategies.

Keywords

k-space formalism • Fourier transform • Spatial resolution • Field-of-view • Sampling • Receiver bandwidth • Spatial frequency • Sampling trajectory

This chapter will review the principles of data acquisitions in frequency space along with the implications that the choice of acquisition parameters, such as sampling frequency and receiver bandwidth, have on the resulting image parameters such as spatial resolution, field-of-view (FOV), spatial aliasing, and others. The k-space formalism also allows for a convenient and intuitive interpretation of sampling patterns, usually referred to as k-space trajectories, through the use of pulsed magnetic field gradients. This concept will be discussed along with standard rectilinear or Cartesian sampling and examples of echo-planar MRI as well as radial and spiral trajectories. For a more extensive derivation of these concepts and the underlying mathematics, the interested reader is referred to textbooks [1–3].

M. Loecher, PhD
Department of Medical Physics, University of Wisconsin-Madison, 1111 Highland Ave, Suite 1127, Madison, WI 53705-2275, USA

O. Wieben, PhD (✉)
Department of Medical Physics, University of Wisconsin-Madison, 1111 Highland Ave, Suite 1127, Madison, WI 53705-2275, USA

Department of Radiology, University of Wisconsin-Madison, 1111 Highland Ave, Suite 1127, Madison, WI 53705-2275, USA
e-mail: owieben@wisc.edu

Introduction to k-Space

The ultimate goal in MR imaging is the generation of a diagnostically useful image that represents the spatial distribution of certain tissue properties as influenced by the spin distribution, relaxation parameters, and physiological factors such as flow, motion, and diffusion. Some early MRI approaches exploited pointwise scanning of the object [4]. This method is very time-consuming and extremely

M.A. Syed et al. (eds.), *Basic Principles of Cardiovascular MRI: Physics and Imaging Technique*,
DOI 10.1007/978-3-319-22141-0_2

limited in its signal-to-noise ratio (SNR) because of the inherently low signal that arises from a single voxel. This approach somewhat resembles the use of a digital camera that has only a single sensor to acquire signal from each individual voxel one after another in a sequential digitization process, instead of the actual simultaneous use of many light receptors.

Instead, MR data acquisition is conducted in a transform domain called *Fourier space*, which is also called *frequency space*. In MRI, this domain is commonly referred to as *k-space* based on nomenclature established by physicists and mathematicians to describe spatial frequencies in equations that contain propagating waves such as light, sound, or radio waves [5]. This terminology precedes its use in MR imaging, and the letter '*k*' is neither an abbreviation nor does it have a specific meaning.

Acquiring data in an alternative domain is not necessarily intuitive at a first glance, but can offer many advantages. This approach is not uncommon in medical imaging; consider, for example, the use of the Radon transform for Computed Tomography (CT) image reconstruction from projection data. One tremendous advantage of k-space acquisition is that the net magnetization in every voxel of the imaging volume contributes to the received signal simultaneously, thereby greatly amplifying the SNR and scan efficiency. While many transforms share this property, MR data acquisition is conducted in Fourier space because the time-varying gradient waveforms used for imaging give rise to a signal equation that directly resembles the Fourier transform (FT) and therefore ensures a straightforward image reconstruction using 2D or 3D FT as shown in Fig. 2.1. This is somewhat of a fortunate coincidence for the field of MRI and the realization of the k-space formalism [6–8] has greatly advanced the field.

Signal Equation and k-Space

We can represent an extremely simplified MRI signal equation as:

$$S(t)=\iiint I(\boldsymbol{r})e^{i\gamma \boldsymbol{r}\cdot\int_0^t \boldsymbol{G}(t')dt'} d^3r \tag{2.1}$$

Where $S(t)$ is the free-induction decay (FID) or echo detected by an RF receiver coil; $\boldsymbol{I(r)}$ describes the signal associated with spatial location or point $\mathbf{r}$, which is dependent on several factors including proton density, T_1 and T_2 relaxation, as well as imaging parameters; i is the imaginary unit; γ is the nuclear gyromagnetic ratio; and $\boldsymbol{G}(t)$ is a vector quantity that represents the magnetic field gradient at time t after the magnetic excitation. We can then substitute:

$$\boldsymbol{k}(t)=\gamma\int_0^t \boldsymbol{G}(t')dt' \tag{2.2}$$

to simplify Eq. 2.1 and we obtain:

$$S(t)=\iiint I(\mathrm{r})e^{i\mathrm{k}(t)\cdot\mathrm{r}}d^3r \tag{2.3}$$

where we can see the relationship between the acquired signal, $S(t)$, the original object, $I(\boldsymbol{r})$, and the spatial-frequency distribution, $\boldsymbol{k}(t)$.

In this notation, the signal equation which links the data acquired with the RF receiver coil to the spatial distribution of the underlying MR signal sources resembles the Fourier transform. Mapping the acquired FID to its corresponding value of $k(t)\cdot r$ gives us our k-space representation, where the acquired time varying data is mapped onto a spatial frequency coordinate system relating it to the applied gradients. In this context, the k-space representation can be either two

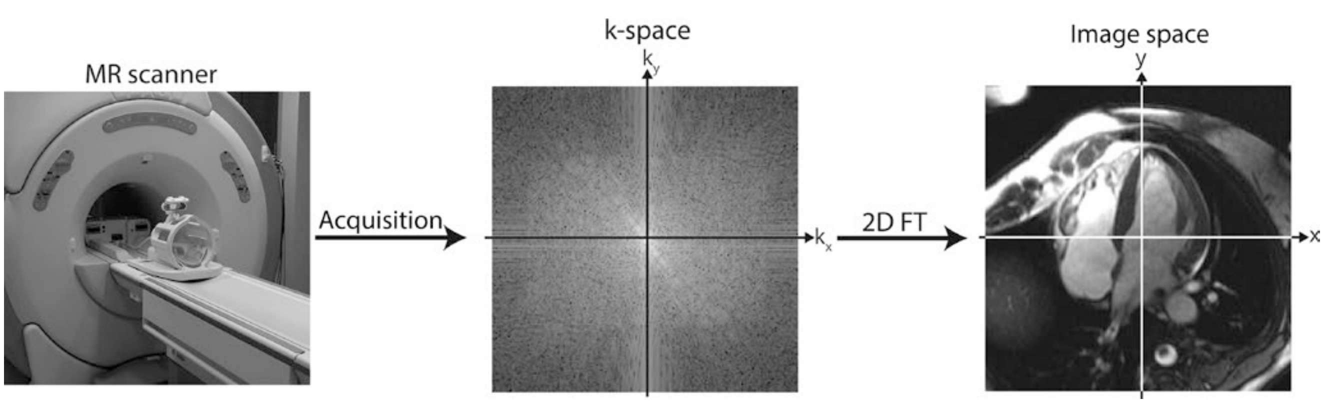

Fig. 2.1 The acquisition and reconstruction process for MR imaging. Data is collected using RF receiver coils. Through the use of time varying gradients, the data are acquired in Fourier space, also commonly referred to as k-space. A Fourier transform (FT) is required to reconstruct the desired image that displays the signal distribution in spatial coordinates

or three dimensional, depending on the acquisition scheme. In general, $\boldsymbol{k}(t)$ has three directional components, commonly notated as kx, ky, and kz. The acquired k-space data points are complex valued and correspond to spatial frequencies with units of 1/distance.

Spatial Frequencies

The acquisition of the weighting coefficients of spatial frequencies is central to MR imaging as it is based on the concept that any image can be represented in Fourier space as a weighted sum of harmonic functions of multiple spatial frequencies and orientations. Thereby, the data representation in image space and frequency space are linked with the Fourier transform [3].

This relationship is illustrated in Fig. 2.2, where the underlying patterns of three representative spatial harmonics are explored in more detail. Datapoint (O) represents the weighting coefficient for a low spatial frequency in the *ky-direction* and the zero spatial frequency in the *kx*-direction. The spatial frequency is inversely proportional to the wavelength. Consequently, it represents a wave pattern of moderately long wavelength, λ_O, which is strictly oriented along the y-axis. Datapoint (P) has components in *kx* and *ky* and represents a diagonal wave pattern, here of higher spatial frequency with a shorter wavelength, λ_P. Datapoint (Q) is a special case as it represents the origin of the coordinate system, which corresponds to the sum of the signal in the image across all voxels, thereby reflecting the average signal intensity of the image when properly scaled. The resulting image is composed of the sum of all wave patterns weighted by the coefficient (grayscale value) in the k-space representation. It can be shown that any image can be accurately decomposed into the sum of these weighted wave patterns with varying wavelengths and angle orientations. The weighting coefficients of the wave patterns are displayed in grayscale as the k-space representation of the image.

Data Properties in Image Space and k-Space

In MRI, the k-space data, also referred to as the raw MR data, are directly measured and the corresponding image space is reconstructed by performing an inverse 2D or 3D Fourier transform. It is noteworthy that the process is reciprocal: for a known image, forward FT can generate the corresponding k-space representation, a fact that can be important for example in certain iterative reconstructions. It is further important to note that the Fourier transform generally generates complex valued data in both domains. In MR imaging, the acquired k-space signal is complex valued as it is obtained with quadrature coils containing a real and an imaginary channel. The MR image is also complex valued due to various factors including magnetic susceptibility, chemical shift, data inconsistencies from motion and flow artifacts, acquisition imperfections such as eddy currents and gradient delays, and other factors that cause the image to deviate from what would ideally be real-valued.

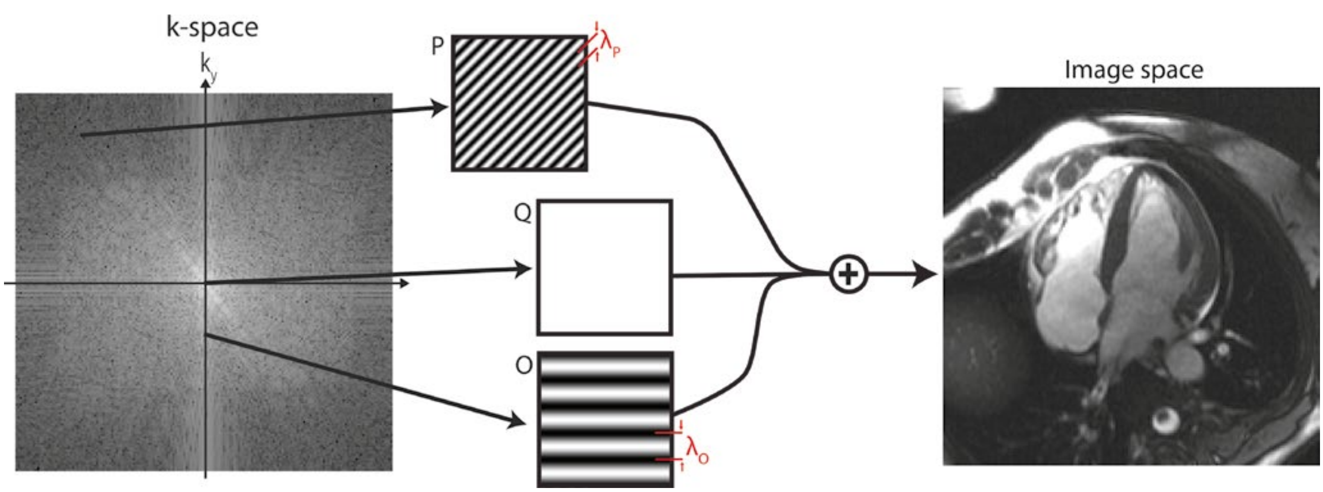

Fig. 2.2 A visual interpretation of the use of spatial harmonics to decompose an image. Every individual point in k-space represents a spatial frequency that can be represented as a wave of a certain frequency and corresponding wavelength, λ, as well as direction of the wave pattern. The image can be formed by the summation of all wave patterns weighted by their k-space coefficient, which is represented as a grayscale value in the k-space map. Representative pictures of the spatial harmonics are shown for select points O, P, and Q, with their corresponding wavelengths, λ_O and λ_P

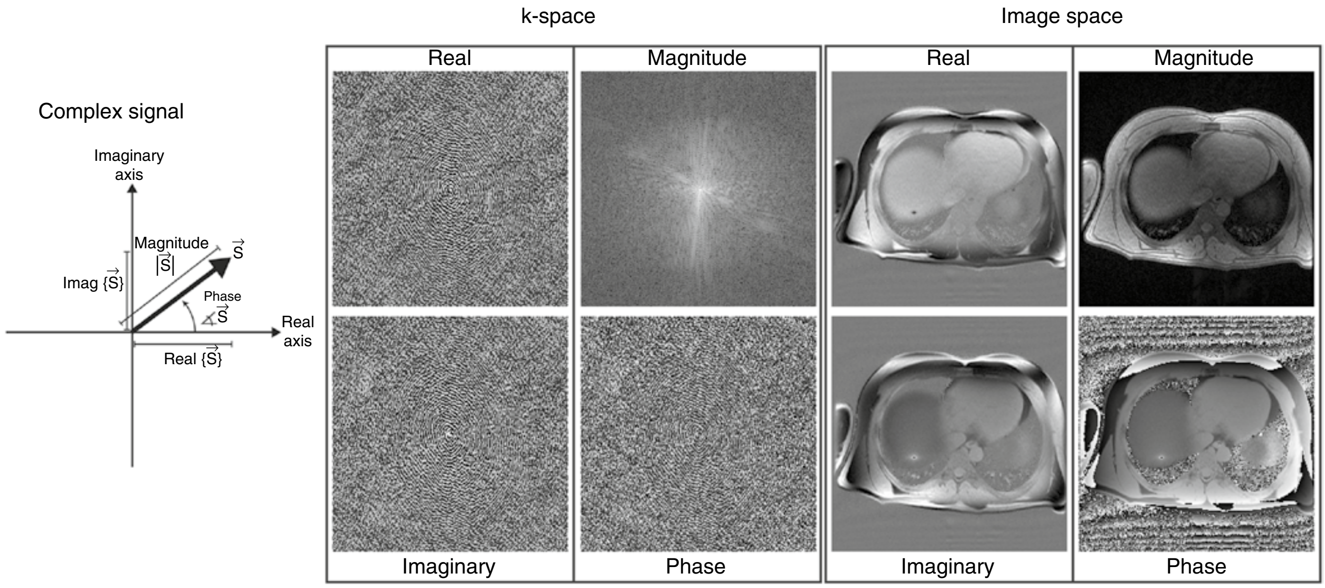

Fig. 2.3 All data from an MR system with quadrature RF coils are complex valued and can be described either by their magnitude and phase or by their real and imaginary components. Often, the image display and storage is reduced to the magnitude display. The in vivo head scan shows that an MR image is not real valued as there are phase contributions from system imperfections and effects such as magnetic susceptibility, motion, and flow

Consequently, a complete data representation in k-space or in image space requires the display of either the real and imaginary channel, or an equivalent display of magnitude and phase of the complex valued signal as shown in Fig. 2.3. The reconstruction process always generates a complex valued image data set. However, in most clinical scans the phase image is discarded and only the magnitude image is utilized for diagnosis. There are some exceptions where diagnostic information is contained in the phase data, including phase contrast MRI, MR elastography, susceptibility weighted imaging, spectroscopy, and fat-water imaging approaches. These techniques require the processing of the phase data in image space in addition to the magnitude data. Alternatively, the data can be stored as a real and an imaginary channel from which magnitude and phase can be derived as shown in Fig. 2.3.

As described above, the center spatial frequency, also called the DC component because it reflects a non-varying image component similar to a direct current, represents the sum of the signal in all voxels in image space. Consequently, it is a very high signal, usually orders of magnitude higher than almost all other k-space coefficients. It is typical in MR images for most of the signal energy to be concentrated in the lower spatial frequencies because the imaging scene is dominated by large, high contrast objects. Therefore, the k-space data are commonly displayed with a logarithmic grayscale as shown in Fig. 2.4. Otherwise, the dynamic range of the display is not sufficient to distinguish signal variances in the lower signal regions, i.e., the outer regions of k-space. The k-space data are usually displayed in the form of a magnitude representation since there is little added value to the human observer to display the k-space phase, or to display the real and imaginary channels. The most essential information, namely the distribution of energy in k-space, is contained in the magnitude component. Nonetheless, it is essential for the reconstruction engine to use complex-valued k-space data and not the magnitude alone.

Matrix Sizes and Artifacts

When using the Fourier transform, the matrix sizes in both domains are identical. In a 2D case, MxN k-space data points are mapped onto MxN image space data points. However, this one-to-one mapping does not always hold true as we introduce acceleration techniques, which allow us to reconstruct more image pixels from less acquired data under certain assumptions, as will be explored in greater detail in Chap. 5. It is important to note that this one-to-one mapping does not mean that a specific data point in k-space reconstructs to a specific data point in image space. In fact, each single point in k-space will influence *all* of the pixels in image space, because each value in k space represents a harmonic function over the whole image. This concept is essential in understanding and identifying some of the artifacts found in MRI, such as those described in Fig. 2.5.

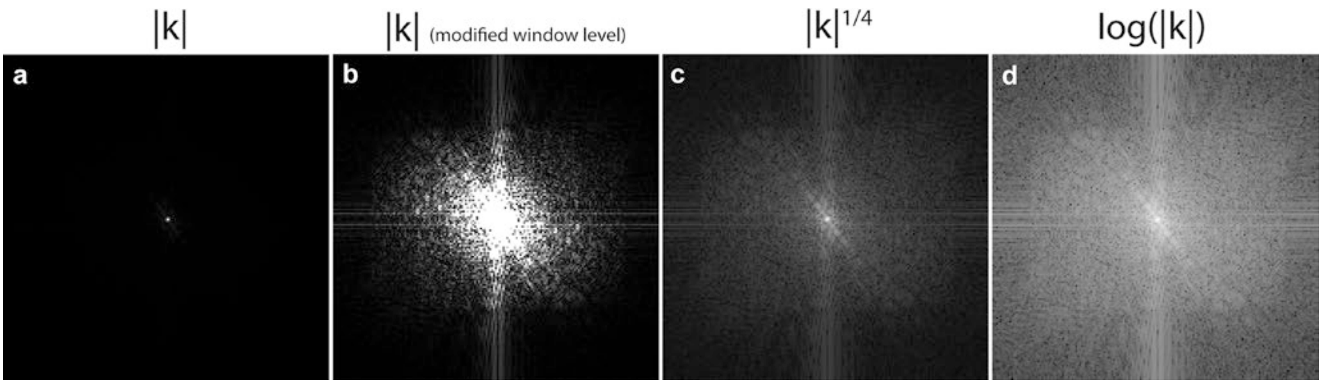

Fig. 2.4 k-space magnitude displays of the cardiac scan shown in Fig. 2.2 with various scaling schemes. As the center of k-space can be on the order of 10,000 times greater than the edges of k-space, a nonlinear display of the grayscale can be advantageous. (**a**) k-space values linearly mapped to greyscale values and using the full dynamic range of the acquired data, which suppressed any signal outside the very center of k space. (**b**) Same as (**a**), except window and level settings have been changed to cap off higher signals to better appreciate lower values. (**c**, **d**) Data scaling with an exponential or logarithm scale can improve the visualization of the smaller values as seen in the higher spatial frequency components

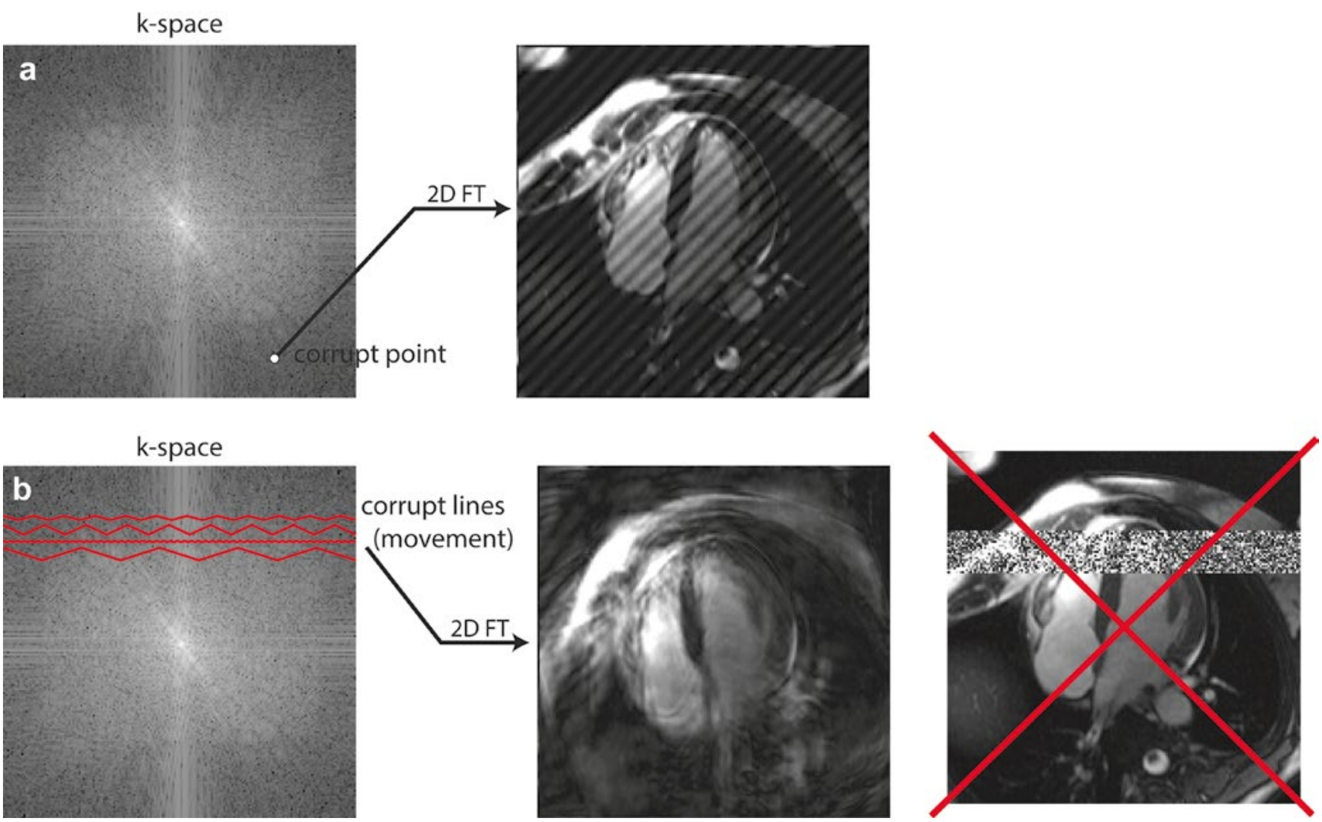

Fig. 2.5 Errors in k-space manifest in image space based on the spatial frequencies affected. (**a**) If a single point in k-space is corrupt, that particular spatial frequency will appear enhanced or reduced in the reconstructed image as shown in this "corduroy" or "spiking" artifact. (**b**) If a patient moves during an acquisition, those portions of k-space will be corrupt and can lead to decreased image quality. These errors will be reflected in the whole image and not only in a single region of the image as shown here for illustration purposes